

# Coherence time of over a second in a telecom-compatible quantum memory storage material

Miloš Rančić,<sup>1,\*</sup> Morgan P. Hedges,<sup>2</sup> Rose L. Ahlefeldt,<sup>1</sup> and Matthew J. Sellars<sup>1</sup>

<sup>1</sup>*Centre for Quantum Computation and Communication Technology,  
Laser Physics Centre, The Australian National University,  
Canberra, Australian Capital Territory 0200, Australia.*

<sup>2</sup>*Physics, Princeton University, Princeton, New Jersey 08554, USA.*

Quantum memories for light will be essential elements in future long-range quantum communication networks. These memories operate by reversibly mapping the quantum state of light onto the quantum transitions of a material system. For networks, the quantum coherence times of these transitions must be long compared to the network transmission times, approximately 100 ms for a global communication network. Due to a lack of a suitable storage material, a quantum memory that operates in the 1550 nm optical fiber communication band with a storage time greater than 1 us has not been demonstrated. Here we describe the spin dynamics of  $^{167}\text{Er}^{3+}:\text{Y}_2\text{SiO}_5$  in a high magnetic field and demonstrate that this material has the characteristics for a practical quantum memory in the 1550 nm communication band. We observe a hyperfine coherence time of 1.3 seconds. Further, we demonstrate efficient optical pumping of the entire ensemble into a single hyperfine state, the first such demonstration in a rare-earth system and a requirement for broadband spin-wave storage. With an absorption of 70 dB/cm at 1538 nm and  $\Lambda$  transitions enabling spin-wave storage, this material is the first candidate identified for an efficient, broadband quantum memory at telecommunication wavelengths.

Any future globally deployed quantum communication network [1, 2] will require nodes connected by optical fiber. To minimize transmission loss and maintain high data throughput, all elements of such a network, particularly quantum repeater nodes, should transmit in one of the low loss telecom bands for optical fiber at 1310 and 1550 nm. In its simplest implementation, a quantum repeater relies on an efficient, long-lived quantum memory [3].

Developing such a memory has proven very challenging. None of the proposed systems that operate directly in the low loss telecom band have the potential for long-term storage [4, 5]. For this reason, more complex ways of interfacing these candidate quantum memories with telecom are being investigated, including frequency conversion [6–9] or non-degenerate photon pairs [10–14].

One of the most promising candidate memory systems

is rare earth ions in solids. The potential for developing practical memories in these systems has been highlighted through a series of recent demonstrations using non-Kramers ions (ions with an even number of electrons). Crystals doped with either praseodymium or europium have demonstrated storage on long lived spin states [15–17], multimode storage [15, 18], large efficiencies [19, 20] and hyperfine coherence times of 6 hours using the Zero First Order Zeeman (ZEFOZ) technique [21]. These demonstrations were successful because the electronic angular momenta of non-Kramers ions can be quenched by the crystal field for sites with sufficiently low symmetry. Therefore, these ions can exhibit the long ground-state hyperfine lifetimes necessary for efficient optical spin pumping and long hyperfine coherence times. These properties are key to the successful operation of efficient, long lived quantum memories. Unfortunately for communication applications, none of the non-Kramers ions have suitable optical transitions in any of the fiber telecom bands.

Compatibility with the telecom bands is offered by Kramers ions, with an odd number of electrons. In particular, erbium has an optical transition in the telecom band at 1538 nm. However, it is much more difficult to make quantum memories with Kramers ions, and not a single Kramers system has demonstrated an on-demand quantum memory. The root of the difficulty is that, unlike for non-Kramers ions, the electronic magnetic moment of Kramers ions cannot be quenched by a crystal field as they possess a half-integer spin. For these ions there is a rapid electronic spin relaxation which shortens the hyperfine state lifetimes. Baldit et al. found the hyperfine state lifetimes to be limited to 100 ms when demonstrating electromagnetic induced transparency in  $^{167}\text{Er}^{3+}:\text{Y}_2\text{SiO}_5$  [22]. This is similar to the electron spin lifetime [23] and only an order of magnitude longer than the optical excited state lifetime, making efficient optical spin pumping very difficult. While some other Kramers ions such as Nd offer shorter optical lifetimes and so slightly improved spin pumping, the electron-spin limit on the hyperfine lifetime is still very short (100ms) preventing long term storage [24]. In comparison, the hyperfine lifetimes for  $\text{Pr}^{3+}:\text{Y}_2\text{SiO}_5$  and  $\text{Eu}^{3+}:\text{Y}_2\text{SiO}_5$  are 5 minutes and 23 days respectively [25, 26].

Nevertheless, the advantage of direct telecom compatibility means there has been considerable work towards developing quantum memories using erbium. Instead of storing on spin states, this work has largely focused on storing on

---

\* Corresponding author: (milos.rancic@anu.edu.au)

the optical transitions. Atomic Frequency Comb (AFC) delay lines have delayed quantum states of light in Er doped glass fiber [5], however, the efficiency was limited to  $\sim 1\%$  and the storage time to 50 ns. Weak coherent states have also been stored in crystals using a two-level Gradient Echo Memory (GEM) technique with an efficiency of 0.25%. The fidelity of the recalled state in this demonstration was, however, well below the non-classical limit [27]. For both these demonstrations the inefficiency of the optical pumping of the ground state electron spin levels was identified as limiting the memories' efficiency. To avoid this limitation, new on-demand memory techniques not requiring optical pumping to initialize the ensemble have been proposed [28, 29] and demonstrated [29]. Although the latter technique has shown significantly higher efficiencies, up to 40%, the storage times are still limited by the optical coherence time and quantum storage has yet to be demonstrated. Currently, there is no proposed strategy to achieve the fidelities and storage times required for quantum repeater applications [30] without using long lived hyperfine states.

Here, we investigate the hyperfine spin dynamics of  $^{167}\text{Er}^{3+}:\text{Y}_2\text{SiO}_5$  in the presence of a large magnetic field, with the aim of increasing both the hyperfine lifetime and coherence time to be comparable to non-Kramers systems. As mentioned above, the hyperfine lifetime is short because it is coupled to the electron spin, which itself flips rapidly due to coupling to the lattice and to other electron spins. In order to increase the hyperfine lifetime, therefore, it is necessary to slow the electron spin flips. Böttger et al. previously demonstrated that a large magnetic field can suppress electronic relaxation in  $\text{Er}^{3+}:\text{Y}_2\text{SiO}_5$  [31]. The field decreases both the electronic spin-lattice coupling and electronic cross-relaxation. The spin-lattice is turned off because, with the electron spin splitting much larger than  $kT$ , the energy density of available phonons is low (see Figure 4). In other words, the electron spin is frozen into the lower spin state. This also turns off the cross-relaxation, since there are no ions in the upper spin state for the polarised ions to cross-relax with. Although the spin is frozen, the lifetime of the excited electron spin state is, in fact, shorter than at low field because of the large density of empty phonon modes available for an excited spin to decay into. This short lifetime has limited the usefulness of this technique for previous memory demonstrations [27, 32]. However, these demonstrations worked with the  $I = 0$  Er isotopes, and here we show that the situation is very different for  $^{167}\text{Er}$  with  $I = 7/2$ . Once the electron spin is frozen in the lower ground state, the hyperfine levels associated with this state can have extremely long lifetimes and coherence times.

The material used for this investigation was a 0.005% doped  $^{167}\text{Er}^{3+}:\text{Y}_2\text{SiO}_5$  crystal, enriched to 92% isotopic purity. The Er ions substitute for Y ions in two non-equivalent  $C_1$  symmetry sites, and this work used the site labelled 'site 2' [33]. To most easily access the regime where the electron spin was frozen, the magnetic field was applied along a direction with a large ground state Zeeman splitting, the  $D_1$

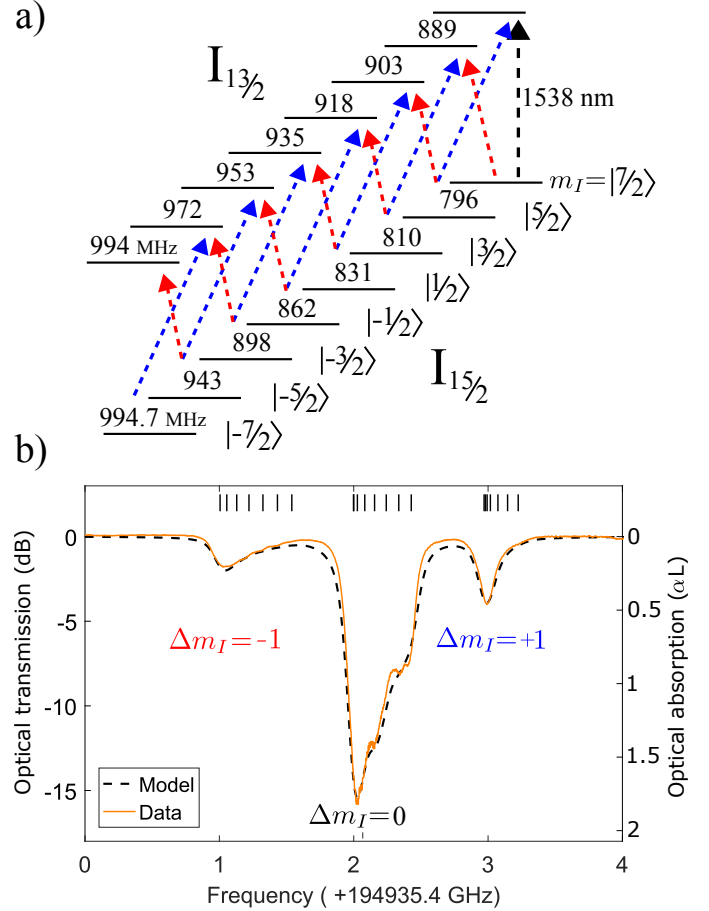


Figure 1. 1538 nm optical transition of  $^{167}\text{Er}^{3+}:\text{Y}_2\text{SiO}_5$  a) Energy level diagram for a field of 7 T. The red-detuned  $\Delta m_I = -1$  transitions are represented by red arrows, and blue arrows for  $\Delta m_I = +1$ . The energy spacing between the hyperfine states was determined by holeburning. b) **Orange:** Absorption spectrum at 1.4 K with a field of 7 T along the  $D_1$  axis. **Black:** model of absorption based on holeburning measurements. **Vertical Black Dashes:** The centroids of the optical transitions used in the black spectrum model.

optical extinction axis (214 GHz/T).

The ground state hyperfine structure was studied optically by exciting the  $4I_{15/2} \rightarrow 4I_{13/2}$  optical transition between the two spin-down projections of the lowest crystal field levels, at a wavelength of 1538 nm (see supplementary materials for the energy level structure). In a field of 7 T, the Zeeman splitting of the electronic spin projections is more than sufficient to resolve this transition. With a nuclear moment of  $I = 7/2$ ,  $^{167}\text{Er}$  exhibits eight hyperfine spin states  $m_I = \{-7/2, \dots, +7/2\}$  and the entire system studied comprises sixteen energy levels, as shown Figure 1 a). The hyperfine energy spacings were obtained by hole-burning measurements (see supplementary materials).

The absorption spectrum of the optical transition is shown in Figure 1 b). Three bands are clearly resolved in this spectrum, which we associate with the  $\Delta m_I = -1, 0$

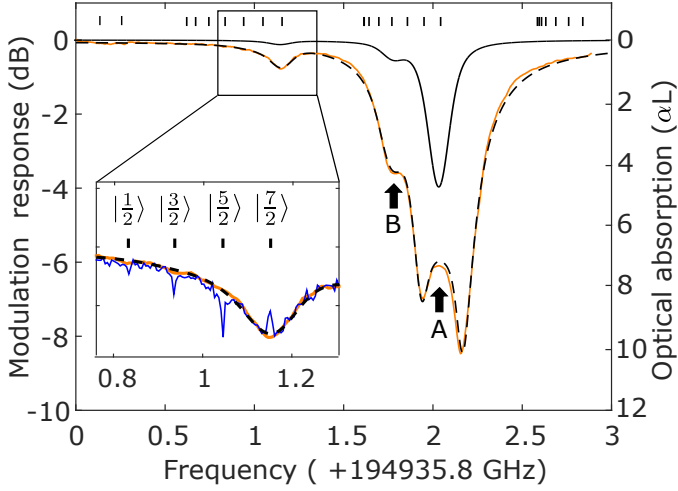


Figure 2. Absorption spectrum of  $^{167}\text{Er}^{3+} : \text{Y}_2\text{SiO}_5$  with 95% of the ensemble pumped into the  $|+7/2\rangle$  hyperfine spin state (Orange, vertical axis on left), obtained by AM spectroscopy. Pumping into the  $m_I = +7/2$  state was achieved by sweeping the light over the set of  $\Delta m_I = +1$  transitions, corresponding to the 2.4 - 3.0 GHz frequency region. Arrow A indicates the center of the  $|+7/2\rangle \rightarrow |+7/2\rangle$  absorption line. Arrow B indicates absorption of isotopic impurities. **Black Solid Trace:** Theoretical model of optical absorption, corresponding to the vertical axis on the right. **Black Dashed Trace:** Theoretical model of the amplitude modulation response. **Black Vertical Dashes:** Centroids of inhomogeneously broadened optical transitions, upon which the model is based, as well as the last two  $\Delta m_I = -2$  transitions on the far left. **Inset (Orange):** An expanded view of the  $\Delta m_I = -1$  transitions. **Inset (Dark Blue):** Upon holeburning at the peak absorption shown by arrow A, a hole and a series of anti-holes are generated at the predicted energies. The labelled dashes indicate the hyperfine ground state for each transition.

and 1 transitions. The splitting between bands is 1 GHz, and they can still be resolved at fields as low as 1 T. The absorption spectrum was fitted with a population model, shown in the figure, based on the measured energy level structure and including the contribution of  $I = 0$  impurity isotopes. The fitted lineshape was a Voigt profile with equal Gaussian and Lorentzian contributions and a linewidth of 150 MHz. The fit was used to determine the oscillator strengths of each hyperfine transition. Whilst the strongest optical transitions have  $\Delta m_I = 0$ , there is appreciable oscillator strength in the fourteen  $\Delta m_I = \pm 1$  transitions. Relative to the  $\Delta m_I = 0$  transitions, the oscillator strengths for  $\Delta m_I = -1$  (+1) start at approximately 25% (31%) for transitions involving the  $| -7/2\rangle$  states, and decrease linearly to about 2.5% (3.1%) for the  $|+7/2\rangle$  states. The decrease can be attributed to a difference in mixing between hyperfine levels across the series.

With the  $\Delta m_I = -1$  and  $+1$  bands clearly resolved, pumping of the nuclear spin into a single state is possible through frequency selection. By exciting only the seven  $\Delta m_I = +1$  transitions (the peak at 3 GHz in Figure 1 b),

we were able to pump  $95 \pm 3\%$  of the  $^{167}\text{Er}$  population into the  $|+7/2\rangle$  hyperfine ground state. This results in a nearly eight-fold increase in the already high optical depth of this transition. Such a high optical depth is difficult to measure accurately with traditional absorption spectroscopy, and instead Amplitude Modulation (AM) spectroscopy was used. This method is sensitive to both the absorption and the phase shift of the transmitted light, allowing a more accurate determination of the optical depth (for more detail, refer to the Materials and Methods section).

The resulting spectrum is shown in Figure 2. Also shown in this figure is the model fitted to the spectrum to obtain the optical depth, and the resulting absorption lineshape. This absorption line has two components – a shoulder at arrow B due to the impurity isotopes, and a central peak at A due to ions in the  $m_I = +7/2$  state. The AM spectrum for this peak has a central dip due to the changing phase of the transmitted light as the laser was swept through the highly absorbing peak. At this frequency the absorption was determined to be  $70 \pm 4$  dB/cm.

When hole-burning at the frequency of arrow A, the blue spectrum in the inset of Figure 2 is observed. The hole and anti-holes demonstrate that spin-pumped population is shifted into  $|+5/2\rangle$ ,  $|+3/2\rangle$  and  $|+1/2\rangle$  hyperfine levels via the  $\Delta m_I = -(1, 2 \& 3)$  optical decay paths.

The efficiency of the spin-pumping ( $95 \pm 3\%$ ) was measured by the fitting the model to only the  $\Delta m_I = -1$  transitions, where the decreasing trend in oscillator strengths and low absorption improve the accuracy of the population estimate. The ability to polarize the  $^{167}\text{Er}$  ensemble into a single hyperfine state opens the path towards several high-bandwidth memory techniques, which are discussed later.

Once the  $^{167}\text{Er}$  ensemble is pumped into the  $|+7/2\rangle$  hyperfine state, the population slowly relaxes to thermal equilibrium via spin-lattice coupling. Three main processes can contribute to this relaxation: the one-phonon direct process, and the two-phonon Raman and Orbach processes [34].

A general expression for the relaxation is:

$$\gamma(T) = \gamma_d T + \gamma_r T^9 + \gamma_{or} f^3 \exp\left(-\frac{hf}{kT}\right) \quad (1)$$

where  $f$  is the ground state electronic splitting.

To first order, these processes only cause decay through the  $\Delta m_I = \pm 1$  hyperfine transitions. This allowed us to model the population dynamics as a series of coupled rate equations, with the same coupling rate  $\gamma$  between all adjacent hyperfine states (see supplementary materials for more information). This population-dynamics model accurately fit the recorded time series of spectra, hence supporting the assumptions of the dynamics.

The resulting time dependence of the spin-lattice relaxation rate is shown in Figure 3. The figure shows an exponential increase in  $T_1$  from 2.2  $\rightarrow$  1.8 K. This agrees with the exponential reduction in high energy phonons associated with the Orbach process. Meanwhile, the plateau

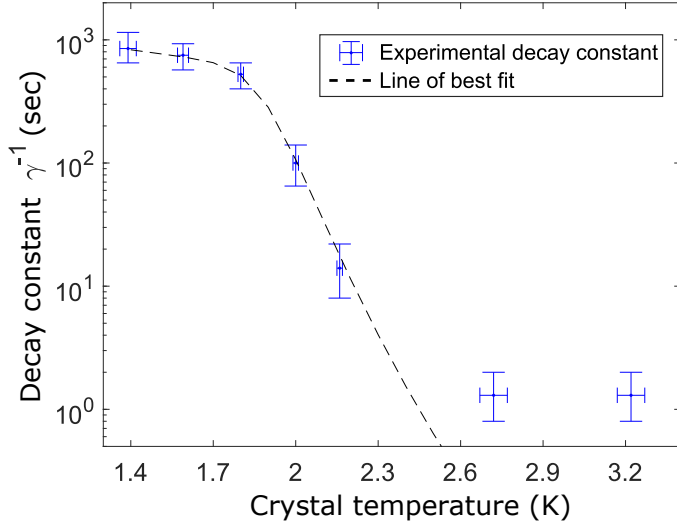


Figure 3. The decay rate of  $^{167}\text{Er}^{3+}$  nuclear spin polarization as a function of temperature, in a field of 7 T. The value of  $\gamma^{-1}$  is the hyperfine population decay rate ( $T_1$ ).  $x$ -axis error bars show the maximum temperature variation during the measurement.  $y$ -axis error bars are given by the fit whose Root Mean Square Deviation (RMSD) is twice as large as the RMSD of the optimal fit to the spectrum.

in transition lifetimes below 1.8 K can be attributed to the direct phonon process. Fitting Equation 1 to the low temperature data gave direct and Orbach coefficients of  $\gamma_d = 9 \times 10^{-4} \text{ s}^{-1} \cdot \text{K}^{-1}$  and  $\gamma_{or} = 8 \times 10^{-30} \text{ s}^{-1} \cdot \text{Hz}^{-3}$  respectively. Above 2.6 K, the plateau in lifetimes indicates the presence of a phonon bottleneck, limiting the rate of hyperfine relaxation [34], which was not included in the model.

The other important decay mechanism in this system is hyperfine spin-spin cross-relaxation. This process is masked in the previous measurement because it does not redistribute the hyperfine populations, and therefore does not change the population envelope. However, it will affect any measurements operating on a sub-group of the entire ensemble, in particular spectral holeburning, which is a vital component of many quantum memory applications. Therefore, it is important to characterize the cross-relaxation process.

We studied hyperfine cross-relaxation by measuring the lifetime of a spectral hole burnt in the unpolarized spin ensemble as a function of magnetic field. As shown in Figure 4, the hole lifetime is short for fields below 3 T. In this regime, the electron spin is not yet frozen and electron spin effects dominate the hole lifetime. There is a small peak in the lifetime at 0.1 T, corresponding to the field where the electronic Zeeman splitting is large enough that electron spin cross-relaxation has been slowed, but where the phonon energy density is still low. As the phonon density increases, the lifetime drops, increasing only as the density drops back down near zero at around 3 T. Above 3

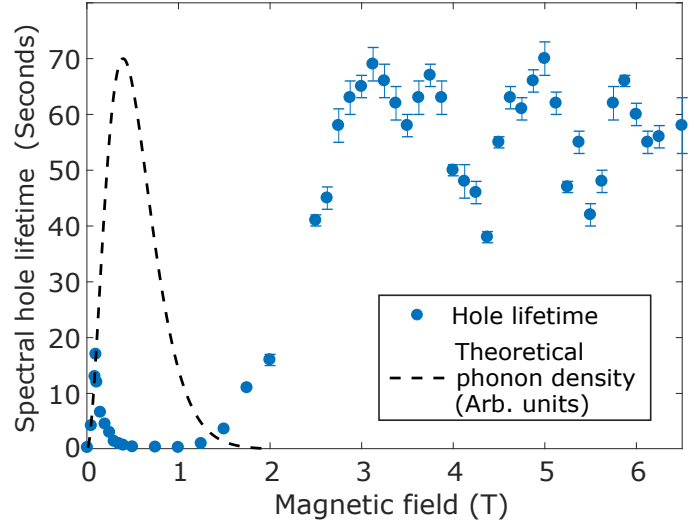


Figure 4. The lifetime of spectral holes burnt into the  $\Delta m_I = +1$  absorption band of  $^{167}\text{Er}^{3+} : \text{Y}_2\text{SiO}_5$  at 1.4 K, as a function of magnetic field along the  $D_1$  axis. The theoretical phonon density in black is a thermal Planck distribution. The curve assumes the Zeeman splitting determined by Guillot-Noël et al [33].  $y$ -axis error bars are the standard error in the fit to each point.

T, hyperfine cross-relaxation dominates the hole lifetime, leading to a maximum lifetime of about 70 s. The hole lifetime does vary with field above 3 T, which is not expected in a simple model of resonant hyperfine cross-relaxation. We attribute the variation to the existence of fields where the detuning between different Er hyperfine transitions can be bridged through hyperfine cross-relaxation mediated by the high concentration of nuclear spin-1/2 Y ions.

These measurements were performed in an unpolarized spin population. In a polarised system, faster cross relaxation will occur for holes burnt into  $\Delta m_I = \pm 1$  states, but if population is transferred to states with  $\Delta m_I = \pm 2$  or higher the cross relaxation will be much slower than seen here.

We have shown that applying a large magnetic field freezes out the electron spin dynamics. This results in a much quieter magnetic environment in the crystal. Since magnetic field fluctuations typically dominate the hyperfine coherence time, this should lead to a substantial increase in the coherence time from its zero field value of 1  $\mu\text{s}$  [22].

We investigated the coherence time on the  $|-7/2\rangle \leftrightarrow |-5/2\rangle$  ground state transition at 7 T using an all-optical Raman echo technique. With this pulse sequence, coherence between hyperfine states is established and manipulated via a common optical excited state, rather than by direct magnetic resonance. The decay of the echo amplitude with time is shown in Figure 5. Below 1 second, the decay is sub-exponential, and the  $e^{-1}$  decay time is  $T_{2(\text{echo})} = 1300 \pm 10$  ms.

With the electron spin frozen, this coherence time will

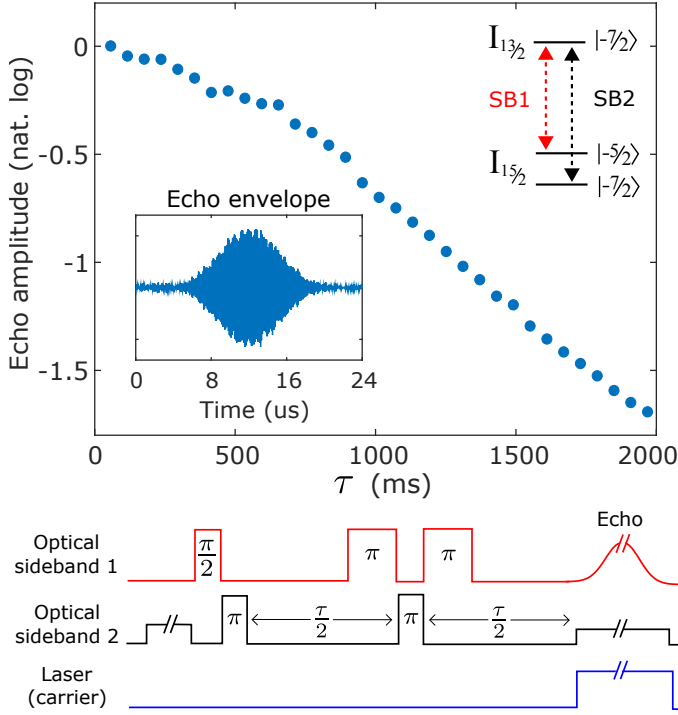


Figure 5. Raman echo measurement of  $^{167}\text{Er}$  coherence time. **Top:** Normalized Raman echo intensity as a function of total delay  $\tau$ , at 1.4 K and 7 T. **Inset:** The Raman echo time envelope with  $\tau = 60$  ms. **Bottom:** pulse sequence for Raman Echoes. The laser sits approximately 1 GHz detuned from the lowest energy transitions, to prevent any absorption. The two optical fields required to drive the ions were provided by the sidebands of the same EOM used for AM spectroscopy, at 1155.3 MHz (SB1) and 2150 MHz (SB2). The carrier acted as a local oscillator to optically detect the Raman echo. SB2 must be on for echoes to form, as it transfers coherence to the optical transition. (Refer to Materials and Methods for more detail).

be dominated by the dynamics of the nuclear spins in the crystal, principally the spin- $1/2$  Y ions. These dynamics are substantially altered from those in undoped  $\text{Y}_2\text{SiO}_5$ . The large magnetic field of the Er ion creates a large frozen core of Y spins whose frequencies are detuned from the bulk [35, 36]. This means that the spin flips of those Y ions having the biggest impact on the Er ion are slowed substantially, resulting in a much longer coherence time than expected if all spins were flipping at the bulk rate (3.6 ms, see supplementary materials for this calculation). The spectral diffusion caused by the slow spin flips of the frozen core also leads to the non-exponential shape to the echo observed in Figure 5.

Here, we have shown that applying a large magnetic field of 7 T can extend the hyperfine coherence time of Er to 1.3 seconds. In fact, Figure 4 indicates that a similar result could be achieved at fields as low as 3 T. 1.3 s is the longest coherence time obtained in any Kramers system, and is comparable to the longest coherence times obtained in non-Kramers systems using the well-known ZEFOZ technique

[21]. From a practical standpoint, the technique shown here has an advantage over ZEFOZ, since it does not require precise alignment of the magnetic field. This technique could be applied to achieve long coherence times in other Kramers ions considered for quantum memories such as Nd [12, 24, 37, 38].

In the context of quantum repeater applications, the coherence time seen here is already sufficient for a large scale network. Razavi et al. show that a coherence time of 1 second is more than sufficient for a 1000 km repeater network, even without error correction [30].

In addition to its long coherence time,  $^{167}\text{Er}:\text{Y}_2\text{SiO}_5$  in the regime studied here has similar optical depth and optical pumping efficiency to  $\text{Pr}:\text{Y}_2\text{SiO}_5$ , the non-Kramers material most widely used for quantum memory demonstrations. It also has 100 times larger hyperfine splittings than Pr, which means that it should have larger memory bandwidths and reduced noise from off-resonant excitation during the memory protocol. Collectively, the parameters presented here suggest  $^{167}\text{Er}$  will rival, or exceed, the performance demonstrated by non-Kramers memories.

This system could also be considered for applications requiring long term storage, i.e: a quantum ‘hard-drive’. For this application, it should be possible to achieve a coherence time approaching the population  $T_1$  limit (10 minutes) at 1.6 K and 7 T using ZEFOZ. To achieve this longer coherence time it is necessary to turn off the hyperfine cross-relaxation. Since cross-relaxation only strongly couples states with  $\Delta m_I = \pm 1$ , it can be eliminated by preparing storage qubits using non-adjacent hyperfine levels, for instance  $|-7/2\rangle \leftrightarrow |-3/2\rangle$ .

Finally, the ability to efficiently pump the  $^{167}\text{Er}$  ensemble into a single hyperfine state is crucial for high-bandwidth quantum communication. It paves the way for broadband Raman memory techniques which, until now, have been limited to atomic vapor systems [39] and potentially nitrogen vacancies in diamond [40]. Alternatively, spin-pumping allows for potentially GHz-bandwidth spin-wave storage using techniques already demonstrated in rare earth systems, such as GEM [19] and drastically improves the efficiency of AFC protocols [41].

## Materials and Methods:

### Experimental Setup

A 0.005% doped  $^{167}\text{Er}^{3+}:\text{Y}_2\text{SiO}_5$   $3 \times 4 \times 5$  mm ( $D_1, D_2, b$ ) crystal provided by Scientific Materials Corp (Bozeman, Montana) was maintained at 1.4 K in an Oxford helium bath cryostat with a 15 T super-conducting magnet (see Figure 1 of the supplementary materials). Both the magnetic field and light propagating direction were parallel with the  $D_1$  optical extinction axis. As there was only one cryostat window, the crystal was placed against a mirror, onto which the beam was focused with a 70  $\mu\text{m}$  waist. The reflection down the  $D_1$  axis gave a total absorption length of 6mm. The optical transitions were excited with



a Thorlabs TLK-1550R laser, stabilized to a home-made fiber reference cavity with a 1 second linewidth less than 100 kHz. Intensity and frequency modulation of the light was achieved with a 10 GHz JDSU AM-EOM and detected with a Lab Buddy 10 GHz detector.

### AM Spectroscopy

This method was based on detecting the optical beat between the sidebands and carrier of an EOM as a function of the modulation frequency. The RF modulation sweep was generated by a spectrum analyzer, which was also used for detection. This formed a closed modulation loop, as shown in Figure 1 of the supplementary materials. The optical sidebands were weak ( $\sim 1\%$ ) compared to the carrier power and the laser was kept far detuned (0.5 – 1 GHz) from the absorption.

This technique is phase sensitive, allowing for accurate measurement of large optical depths, and as the laser remains locked to the reference cavity spectra can be recorded in conjunction with precise optical pulses and sweeps.

### Energy Structure and Spin Pumping

The hyperfine structure of the  $I_{15/2}$  and  $I_{13/2}$  states was determined at 7 T and 1.4 K through a series of holeburning measurements. A 0 to 4 GHz tunable RF source was used to generate a series of 20 spectral holes across 3 sets of measurements (see Supplementary Materials Section 3 for an example spectrum). Each spectrum was made by applying fixed frequency RF for 100 ms. The absorption spectrum was recorded by a 0.01 to 2.9 GHz RF scan with the tracking generator and RF input on the spectrum analyzer (50 ms scan, 1 MHz RBW).

To spin pump the ensemble into either the  $m_I = | +7/2 \rangle$  or  $| -7/2 \rangle$  hyperfine ground state, a Voltage Controlled Oscillator (VCO) was used to drive the EOM. A 3 second saw-tooth scan (100 ms rep rate) was performed over the  $\Delta m_I = -1$  or  $+1$  absorption bands respectively, with  $\sim 2$  mW of optical power in each sideband. The spin-pumped absorption spectrum was recorded once again using AM spectroscopy. Repeating this with the laser (carrier) frequency on either side of the absorption feature, it was possible to stitch two scans together to span more than 2.9 GHz.

### Magnetic Field Dependence of Spectral Holes

Spectral holes were burnt into the center of the  $\Delta m_I = +1$  absorption band, as it afforded higher optical depth than the  $\Delta m_I = -1$  band and deeper spectral holes than the  $\Delta m_I = 0$  band, which had isotopic impurities and excessive optical depth. Between 0 and 1.5 T, spectral holes were generated using a tunable RF source. Above 1.5 T, 10 MHz wide spectral trenches were burnt instead, as there was negligible spectral diffusion and long hole-burning lifetimes. This was achieved by sweeping the spectrum analyzer tracking generator output over 10

MHz for 10 seconds. The tracking generator output was centered at approximately 1.5 GHz to keep the laser carrier and second sideband off-resonant. The spectral features were measured using Phase Modulation (PM) spectroscopy.

### Temperature Dependence of Spin Pumping

In a 7 T field, spin pumping into the  $m_I = | +7/2 \rangle$  state was achieved using the same technique as described above. At each temperature, 4 to 5 spectra were recorded at time intervals spaced long enough to observe appreciable relaxation back to thermal equilibrium. For example, at 1.6 K, spectra were recorded after 10 seconds and (10, 20, 40, 80) minutes. See Section 5 of the Supplementary materials for example spectra.

### Optical Raman Echoes

Optical pulses ( $\pi$  &  $\pi/2$ ) were generated using the EOM sidebands and two RF generators tuned to 1155.3 MHz and 2150 MHz. The pulse lengths were optimized using two pulse optical echoes at either frequency, with 1.5 mW of optical power in each sideband. For the  $|I_{15/2}, -5/2\rangle \leftrightarrow |I_{13/2}, -7/2\rangle$  transition (1155.3 MHz), the optimal  $\pi$ -pulse length is  $4 \pm 0.5 \mu\text{s}$  and for the  $|I_{15/2}, -7/2\rangle \leftrightarrow |I_{13/2}, -7/2\rangle$  a  $\pi$ -pulse was  $1.5 \mu\text{s}$  (2150 MHz). This pair of transitions were chosen because they have the largest oscillator strengths, so shorter pulses could be used. The hyperfine spin ensemble was prepared by first pumping into the  $m_I = | -7/2 \rangle$  state with a VCO for 10 seconds, as described above. This was followed by applying a 100  $\mu\text{W}$  pulse at 2150 MHz for 100 ms, to generate a 100 kHz wide absorption feature (anti-hole) in the  $m_I = | -5/2 \rangle$  subgroup. After the pulse sequence, the echo that reformed at the wavelength of the 1150 MHz sideband was detected as a 1155.3 MHz optical beat between the sideband and the carrier. This RF signal was then mixed with a 1145.3 MHz RF source, and the 10 MHz beat signal was recorded. Note: The detected echo amplitude in this technique depends on the proportion of the initial ensemble transferred into the optical  $| -7/2 \rangle \leftrightarrow | -7/2 \rangle$  transition, which is determined by the probing power of sideband 2.

One advantage of this technique is that the bandwidth of the  $\sim 1 \mu\text{s}$  optical pulses used is much larger than the inhomogeneous broadening of the hyperfine transition, and so the width of the echo envelope gives a direct measure of this inhomogeneous broadening. As shown in the inset to Figure 5, the echoes had a FWHM of  $7 \pm 1 \mu\text{s}$ , corresponding to an inhomogeneous linewidth of  $130 \pm 20$  kHz.

### Data availability

The data that support the plots within this paper and other findings of this study are available from the corresponding author upon reasonable request.

## Acknowledgments

M. J. S would like to thank Charles Thiel for insightful discussions. This work was supported by the Australian Research Council Centre of Excellence for Quantum Computation and Communication Technology (Grant No. CE110001027). M. J. S. was supported by an Australian Research Council Future Fellowship (Grant No.

FT110100919).

## Author Contributions

M. J. S and M. P. H. conceived the initial project. M. J. S, M. P. H and M. R. designed the experimental setup. M. R. carried out the experiment. M. R and R. L. A. analyzed the results. All authors contributed to writing the manuscript

- 
- [1] Gisin, N. & Thew, R. Quantum communication. *Nat. Photon.* **1**, 165–171 (2007).
  - [2] Kimble, H. J. The quantum internet. *Nature* **453**, 1023–1030 (2008).
  - [3] Duan, L. M., Lukin, M. D., Cirac, J. I. & Zoller, P. Long-distance quantum communication with atomic ensembles and linear optics. *Nature* **414**, 413–8 (2001).
  - [4] Riedinger, R. *et al.* Non-classical correlations between single photons and phonons from a mechanical oscillator. *Nature* **530**, 313–316 (2016).
  - [5] Saglamyurek, E. *et al.* Quantum storage of entangled telecom-wavelength photons in an erbium-doped optical fibre. *Nat. Photon.* **9**, 83–87 (2015).
  - [6] Radnaev, A. G. *et al.* A quantum memory with telecom-wavelength conversion. *Nature Phys.* **6**, 894–899 (2010).
  - [7] Dudin, Y. O., Radnaev, A. G., Zhao, R., Blumoff, J. Z., Kennedy, T. A. B. & Kuzmich, A. Entanglement of light-shift compensated atomic spin waves with telecom light. *Phys. Rev. Lett.* **105**, 260502 (2010).
  - [8] Albrecht, B., Farrera, P., Fernandez-Gonzalvo, X., Cristiani, M. & de Riedmatten, H. A Waveguide Frequency Converter Connecting Rubidium Based Quantum Memories to the Telecom C-Band. *Nat. Commun.* **5** 3376 (2014).
  - [9] Maring, N., Kutluer, K., Cohen, J., Cristiani, M., Mazzera, M., Ledingham, P. M., & de Riedmatten, H. Storage of up-converted telecom photons in a doped crystal. *New J. Phys.* **16**, 113021 (2014).
  - [10] Seri, A., Lenhard, A., Rieländer, D., Gündoğan, M., Ledingham, P. M., Mazzera, M., & de Riedmatten, H. Quantum Correlations between Single Telecom Photons and a Multimode On-Demand Solid-State Quantum Memory. *Phys. Rev. X* **7**, 021028 (2017).
  - [11] Saglamyurek, E. *et al.* Broadband waveguide quantum memory for entangled photons. *Nature* **469**, 512–515 (2011).
  - [12] Clausen, C., Usmani, I., Bussieres, F., Sangouard, N., Afzelius, M., de Riedmatten, H., & Gisin, N. Quantum storage of photonic entanglement in a crystal. *Nature* **469**, 508–511 (2011).
  - [13] Bussieres, F. *et al.* Quantum teleportation from a telecom-wavelength photon to a solid-state quantum memory. *Nat. Photon.* **8**, 775–778 (2014).
  - [14] Zhang, W., Ding, D. S., Shi, S., Li, Y., Zhou, Z. Y., Shi, B. S., & Guo, G. C. Storing a single photon as a spin wave entangled with a flying photon in the telecommunication bandwidth. *Phys. Rev. A* **93**, 022316 (2016).
  - [15] Ferguson, K. R., Beavan, S. E., Longdell, J. J. & Sellars, M. J. Generation of Light with Multimode Time-Delayed Entanglement Using Storage in a Solid-State Spin-Wave Quantum Memory. *Phys. Rev. Lett.* **117**, 020501 (2016).
  - [16] Jobez, P., Laplane, C., Timoney, N., Gisin, N., Ferrier, A., Goldner, P., & Afzelius, M. Coherent Spin Control at the Quantum Level in an Ensemble-Based Optical Memory. *Phys. Rev. Lett.* **114**, 230502 (2015).
  - [17] Gündoğan, M., Ledingham, P. M., Kutluer, K., Mazzera, M. & de Riedmatten, H. Solid State Spin-Wave Quantum Memory for Time-Bin Qubits. *Phys. Rev. Lett.* **114**, 230501 (2015).
  - [18] Laplane, C., Jobez, P., Etesse, J., Timoney, N., Gisin, N., & Afzelius, M. Multiplexed on-demand storage of polarization qubits in a crystal. *New J. Phys.* **18**, 013006 (2015).
  - [19] Hedges, M. P., Longdell, J. J., Li, Y. & Sellars, M. J. Efficient quantum memory for light. *Nature* **465**, 1052–1056 (2010).
  - [20] Sabooni, M., Li, Q., Kröll, S. & Rippe, L. Efficient Quantum Memory Using a Weakly Absorbing Sample. *Phys. Rev. Lett.* **110**, 133604 (2013).
  - [21] Zhong, M. *et al.* Optically addressable nuclear spins in a solid with a six-hour coherence time. *Nature* **517**, 177–80 (2015).
  - [22] Baldit, E. *et al.* Identification of  $\Lambda$ -like systems in  $\text{Er}^{3+}:\text{Y}_2\text{SiO}_5$  and observation of electromagnetically induced transparency. *Phys. Rev. B* **81**, 144303 (2010).
  - [23] Hastings-Simon, S. R. *et al.* Zeeman-level lifetimes in  $\text{Er}^{3+}:\text{Y}_2\text{SiO}_5$ . *Phys. Rev. B* **78**, 085410 (2008).
  - [24] Usmani, I., Afzelius, M., de Riedmatten, H., & Gisin, N. Mapping multiple photonic qubits into and out of one solid-state atomic ensemble. *Nat. Commun.* **1**, 1010 (2010).
  - [25] Holliday, K., Croci, M., Vauthey, E. & Wild, U. P. Spectral hole burning and holography in an  $\text{Pr}^{3+}:\text{Y}_2\text{SiO}_5$  crystal. *Phys. Rev. B* **47**, 14741–14752 (1993).
  - [26] Könz, F. *et al.* Temperature and concentration dependence of optical dephasing, spectral-hole lifetime, and anisotropic absorption in  $\text{Eu}^{3+}:\text{Y}_2\text{SiO}_5$ . *Phys. Rev. B* **68**, 085109 (2003).
  - [27] Lauritzen, B., Minár, J., de Riedmatten, H. Afzelius, M., Sangouard, N., Simon, C., & Gisin, N. Telecommunication-Wavelength Solid-State Memory at the Single Photon Level. *Phys. Rev. Lett.* **104**, 080502 (2010).
  - [28] Hétet, G., Longdell, J. J., Alexander, A. L., Lam, P. K. & Sellars, M. J. Electro-Optic Quantum Memory for Light Using Two-Level Atoms. *Phys. Rev. Lett.* **100**, 023601 (2008).

- [29] Dajczgewand, J., Le Gouët, J.-L., Louchet-Chauvet, A. & Chanelière, T. Large efficiency at telecom wavelength for optical quantum memories. *Opt. Lett.* **39**, 2711 (2014).
- [30] Razavi, M., Piani, M. & Lütkenhaus, N. Quantum repeaters with imperfect memories: Cost and scalability. *Phys. Rev. A* **80**, 032301 (2009).
- [31] Böttger, T., Thiel, C. W., Cone, R. L. & Sun, Y. Effects of magnetic field orientation on optical decoherence in  $\text{Er}^{3+}:\text{Y}_2\text{SiO}_5$ . *Phys. Rev. B* **79**, 115104 (2009).
- [32] Kurkin, I. & Chernov, K. EPR and spin-lattice relaxation of rare-earth activated centres in  $\text{Y}_2\text{SiO}_5$  single crystals. *Physica B+C* **101**, 233–238 (1980).
- [33] Guillot-Noël, O., Goldner, P., Du, Y. L., Baldit, E., Monnier, P., & Bencheikh, K. Hyperfine interaction of  $\text{Er}^{3+}$  ions in  $\text{Y}_2\text{SiO}_5$ : An electron paramagnetic resonance spectroscopy study. *Phys. Rev. B* **74**, 214409 (2006).
- [34] Abragam, A. & Bleaney, B. Electron Paramagnetic Resonance of Transition Metal Ions. *Dover Pub.* 2nd Edn, Chapter 10, (1970).
- [35] Böttger, T., Thiel, C. W., Sun, Y. & Cone, R. L. Optical decoherence and spectral diffusion at  $1.5\ \mu\text{m}$  in  $\text{Er}^{3+}:\text{Y}_2\text{SiO}_5$  versus magnetic field, temperature, and  $\text{Er}^{3+}$  concentration. *Phys. Rev. B* **73**, 075101 (2006).
- [36] Guillot-Noël, O., Vezin, H., Goldner, P., Beaudoux, F., Vincent, J., Lejay, J., & Lorgère, I. Direct observation of rare-earth-host interactions in  $\text{Er}^{3+}:\text{Y}_2\text{SiO}_5$ . *Phys. Rev. B* **76**, 180408 (2007).
- [37] Wolfowicz, G., Maier-Flaig, H., Marino, R., Ferrier, A., Vezin, H., Morton, J. J. L., & Goldner, P. Coherent Storage of Microwave Excitations in Rare-Earth Nuclear Spins. *Phys. Rev. Lett.* **114**, 170503 (2015).
- [38] Zhou, Z. Q., Lin, W. B., Yang, M., Li, C. F. & Guo, G. C. Realization of Reliable Solid-State Quantum Memory for Photonic Polarization Qubit. *Phys. Rev. Lett.* **108**, 190505 (2012).
- [39] Saunders, D. J. *et al.* Cavity-Enhanced Room-Temperature Broadband Raman Memory. *Phys. Rev. Lett.* **116**, 090501 (2016).
- [40] Poem, E. *et al.* Broadband noise-free optical quantum memory with neutral nitrogen-vacancy centers in diamond. *Phys. Rev. B* **91**, 205108 (2015).
- [41] de Riedmatten, H., Afzelius, M., Staudt, M. U., Simon, C. & Gisin, N. A solid-state light-matter interface at the single-photon level. *Nature* **456**, 773–777 (2008).